

PAPER • OPEN ACCESS

Prediction of operating offshore wind farms underwater noise from reanalysis of single point underwater noise measurement

To cite this article: Mahardika Firjatullah *et al* 2025 *IOP Conf. Ser.: Earth Environ. Sci.* **1464** 012033

View the [article online](#) for updates and enhancements.

You may also like

- [Analysis of the pump-turbine cavitation with small guide vane opening on pump mode](#)
Q H Tian, H P Min, Y X Xiao *et al.*
- [Material Characterization using Magnetic Induction Based Measurement Technique at Low-Frequency Range](#)
Kurnia Nugraha, Winarto Winarto, Didied Haryono *et al.*
- [A preliminary study of WebGIS-based waste management visualization to support halal tourism areas in Bandung](#)
Qoriah, T Vani, N Simarmata *et al.*



The Electrochemical Society
Advancing solid state & electrochemical science & technology

ECS UNITED

247th ECS Meeting
Montréal, Canada
May 18-22, 2025
Palais des Congrès de Montréal

Early registration deadline: April 21, 2025

Unite with the ECS Community

Prediction of operating offshore wind farms underwater noise from reanalysis of single point underwater noise measurement

Mahardika Firjatullah¹, Irsan Soemantri Brodjonegoro^{2*} and Farid Putra Bakti²

¹ Ocean Engineering Program, Institut Teknologi Bandung, Bandung, Indonesia

² Offshore Engineering Research Group, Faculty of Civil and Environmental Engineering, Institut Teknologi Bandung, Bandung, Indonesia

*E-mail: irsanb@itb.ac.id

Abstract. In renewable energy, offshore wind turbines are increasingly recognized as significant sources of underwater noise, with growing concerns about their impact on marine life. A key noise contributor is the structural vibration from the turbine's gearbox, transmitted through the tower to the water. This study re-analyzes the underwater noise of a single turbine using field measurements from the Utgrunden wind farm. Turbines are modeled as idealized Euler-Bernoulli beams with a lumped mass at the top, and the analytical response serves as a boundary condition for the employed Combined Helmholtz Integral Equation Formula (CHIEF) underwater noise simulation implementation. By matching CHIEF's output to field data using gradient descent, the approach effectively approximates the noise measurements, despite some limitations like proximity, free surface, and bottom reflection. The findings suggest that cumulative noise from the Utgrunden wind farm is detectable several kilometers away, with in- and out-of-phase noise interactions causing fluctuating noise levels near the farm. This method can optimize wind farm layouts to avoid noise peaks in sensitive areas.

1. Introduction

Predicting the underwater noise generated by the operation of a wind farm is a challenging task. Hydrophones are typically placed in several locations to obtain an accurate readout of the underwater noise. However, the amount of data points that one can obtain is highly restricted by the cost of hydrophones, research vessels, and other operational considerations.

Offshore wind farms pose environmental challenges, including increased underwater noise, collision risks, and pollution from vessel traffic. While noise from a single turbine is comparable to typical marine operations and 20–30 dB lower than passing ships [1], [2], the trend of larger, densely clustered farms will need reassessment. Simulations show noise levels amplify with more turbines [3], [4], highlighting the need to understand wind farms' overall underwater noise impact.

This study proposes a methodology to estimate noise distribution in the vicinity of an operational wind farm using only a single field point measurement. The proposed framework is illustrated in Figure 1. The field noise measurement is conducted based on a sequential shutdown

of the wind farm and analyzed to determine the appropriate mode contribution constant at a given structural vibration frequency. Subsequently, the surface velocity distribution is approximated from this information and then utilized as input for the CHIEF boundary element method. The boundary element method is frequently employed in the modeling of underwater acoustics, particularly in military defense research areas, where it is critical for submarines to remain undetected [5]. The same principle is also used to predict noise from propellers, which ultimately contributes to understanding the noise generated by submarines [6].

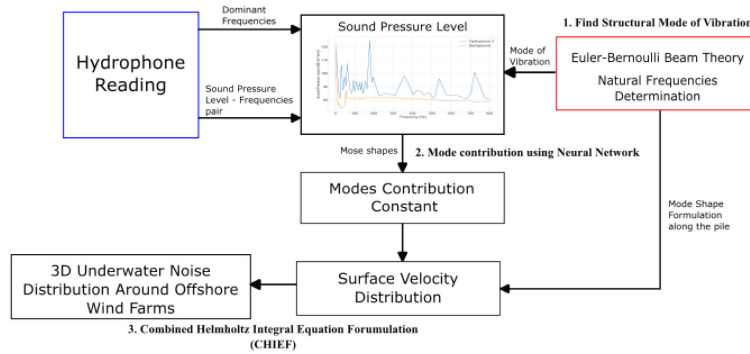


Figure 1. Flow chart describing the framework for predicting 3D underwater noise field.

2. Methodology

2.1 Estimating the monopile modes of vibration [7]

The monopile structure is approximated with an undamped Euler-Bernoulli beam with clamped-free boundary condition and a rigid tip mass affixed to the free-top end with mass of M_t and rotary inertia of I_t . The governing equation of motion for the monopile is presented in Equation 1.

$$YI \frac{\partial^4 w(z, t)}{\partial z^4} + m \frac{\partial^2 w(z, t)}{\partial t^2} = 0 \quad (1)$$

With $w(z, t)$ indicates the transverse displacement at point z along the pile with respect to time t . YI is the bending stiffness, and m is the mass per unit length of the monopile. The clamped-free boundary condition with a tip mass can be expressed by Equation 2 and 3.

$$w(0, t) = 0, \quad \left. \frac{\partial w(z, t)}{\partial x} \right|_{x=0} = 0 \quad (2)$$

$$\left[YI \frac{\partial^2 w(z, t)}{\partial z^2} + I_t \frac{\partial^3 w(z, t)}{\partial t^2 \partial z} \right]_{x=L} = 0, \quad \left[YI \frac{\partial^3 w(z, t)}{\partial z^3} + M_t \frac{\partial^2 w(z, t)}{\partial t^2} \right]_{x=L} = 0 \quad (3)$$

The rotary inertia of the tip mass (I_t) can be approximated using a one-mass model of a wind turbine can be calculated by Equation 4. The general response of the beam is the linear combination of all vibration modes as shown in E Equation 5.

$$I_t = I_r + n_g^2 I_g \quad (4)$$

$$w(z, t) = \sum_{k=1}^{\infty} \left[\cos \frac{\lambda_k}{L} z - \cosh \frac{\lambda_k}{L} z + \zeta_k \left(\sin \frac{\lambda_k}{L} z - \sinh \frac{\lambda_k}{L} z \right) \right] (A_k \cos \omega_k t + B_r \sin \omega_k t) \quad (5)$$

Where A_r and B_r are the unknown constants that can be determined by finding the response to initial conditions $w(z, 0)$ and $\partial w(z, t)/\partial t|_{t=0}$, and ω_k is the eigenfrequency of the k -th vibration mode.

2.2 Combined helmholtz integral equation formulation (CHIEF) boundary element method

2.2.1 CHIEF formulation

An arbitrarily shaped geometry is submerged in an infinite ideal homogeneous fluid that fills the exterior region of the solid surfaces. The fluid has a density of ρ , and the speed of sound on the fluid is c . The fluid fills region exterior to the surface region. Previous studies have indicated that the spatial pressure radiated from vibrating bodies and the normal velocity comply with the Helmholtz integral formulas, as shown in Equation 6, where $p(X)$ is the field pressure, $G(\sigma, X)$ is the green function, $\partial p(\sigma)/\partial n$ is the pressure gradient normal to the body's surface S [10], [11].

$$\int_S \left(G(\sigma, X) \frac{\partial p(\sigma)}{\partial n} - p(\sigma) \frac{\partial G(\sigma, X)}{\partial n} \right) dS = \begin{cases} -p(X) & X \text{ exterior to } S \\ -\frac{1}{2}p(X) & X \text{ on } S \\ 0 & X \text{ interior to } S \end{cases} \quad (6)$$

To evaluate the exterior acoustic pressure using Equation 6, one must provide the entire pressure and normal velocity distribution on the surface S . The pressure gradient may be calculated from the surface velocity distribution as can be found in the surface boundary condition shown in Equation 7, and the field pressure must satisfy the radiation condition [12].

$$\frac{\partial p(X)}{\partial n} = \hat{n}_s \cdot \nabla p(X) = -i\omega\rho v(X), \quad X \in S \quad (7)$$

Upon substituting Equation 7 into Equation 6, the external Helmholtz equation can be transformed into Equation 8. Furthermore, an interior Helmholtz relation is also obtained which can offers a supplementary means to compute the surface pressure, this relation is presented in Equation 9 [13]. In this work, the surface velocity distribution is derived by summing the modes while taking into account the forcing to stiffness term factor obtained through the use of gradient descent, which will be elaborated in Section 2.3.

$$\frac{1}{2}p_m - \sum_{n=1}^{N_s} \left(p_n \int_{S_n} \frac{\partial G(\sigma, X_m)}{\partial n} dS(\sigma) \right) = i\omega\rho \sum_{n=1}^{N_s} \left(v_n \int_{S_n} G(\sigma, X_m) dS(\sigma) \right) \quad (8)$$

$$0 - \int_{S_n} p(\sigma) \frac{\partial G(\sigma, X)}{\partial n} dS(\sigma) = i\omega\rho \int_{S_n} v(\sigma) G(\sigma, X) dS(\sigma) \quad (9)$$

A study have established that the surface Helmholtz integral equation in Equation 8 lacks a unique solution when the wavenumber k coincides or is in proximity to the characteristic

wavenumber k' [11]. However, this limitation does not apply to the interior Helmholtz relation in Equation 9. The CHIEF Method resolves this by combining the surface and interior Helmholtz equations, creating an overdetermined system. The interior equation serves as an additional constraint when k is near the characteristic wave number [14]. The overdetermined system of equations mentioned can be written in matrix form equation Equation 10 with matrices A and B defined in Equation 11 and 12 [15]. The overdetermined system of equations is solved by Householder reduction [16].

$$[A]\{P\} = [B]\{V\} \quad (10)$$

$$A_{mn} = \begin{cases} \frac{1}{2}\delta_{mn} - \iint_{S_n} \frac{\partial G(\sigma, X_m)}{\partial n} dS(\sigma); & m = 1; N_s \\ - \iint_{S_n} \frac{\partial G(\sigma, X_m)}{\partial n} dS(\sigma); & m = (N_s + 1); (N_s + N_I) \end{cases} \quad (11)$$

$$B_{mn} = \begin{cases} i\omega\rho \iint_{S_n} G(\sigma, X_m) dS(\sigma); & SHE \quad m = 1; N_s; 1 \\ i\omega\rho \iint_{S_n} G(\sigma, X_m) dS(\sigma); & IHR \quad m = (N_s + 1); (N_s + N_I); 1 \end{cases} \quad (12)$$

2.2.2 CHIEF numerical implementation

The CHIEF algorithm is implemented in FORTRAN language [15]. The inputs of CHIEF are the geometry of the modeled structure, and the boundary condition in the form of surface velocity distribution. The output produced is the near-field pressure. The validity of CHIEF implementation needs to be tested against an analytic formula, in this validation a uniformly vibrating sphere with radius a and radial velocity of V generates field acoustic pressure that can be calculated using Equation 13 [17].

$$p(r) = \frac{i\omega\rho Va^2 e^{ika} e^{-ikr}}{1 + ika} \frac{1}{r}, r \geq a \quad (13)$$

In this validation, the radius set to be 1 m , and the radial breathing velocity (V) is 1 m/s with wave number (k) of $\pi/3$. The results shown in Figure 2 reveals an average error of 2.22% for various surface discretization size. This validation confirms that the CHIEF numerical tools are suitable for addressing similar pressure radiation issues.

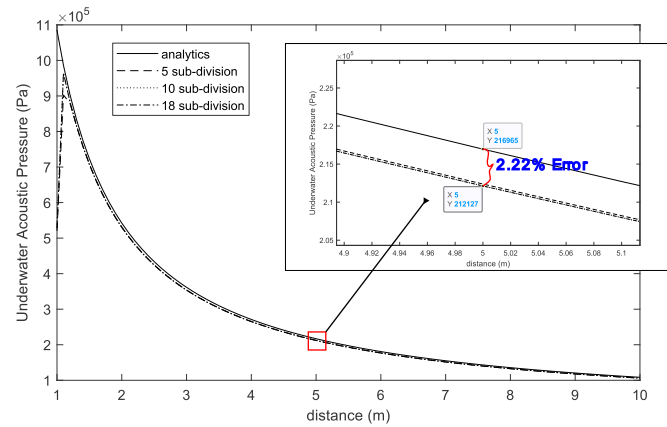


Figure 2. pressure validation for CHIEF implementation to analytical method. The analytical results are compared across various model meshing schemes, demonstrating a relatively consistent error across all schemes.

2.3 Mode contribution determination using gradient descent

In this paper, the problem of determining a hyperparameter of an environmental factor based can be framed as solving an overdetermined system discussed in Section 3.2. To address this issue, the gradient descent algorithm, a first-order optimization method, is proposed to iteratively update hyperparameters in the direction of the objective function's steepest descent. Minimizing the error between sensor readings and predictions based on environmental factors allows for accurate estimation of the factors governing wind turbine vibrations.

The underlying reason behind this method selection is gradient descent method applies to a wide range of penalty functions especially the non-smooth one [19]. Gradient descent can effectively navigate this challenging landscape by following the gradient direction towards the global minimum of the objective function.

In the process of finding the hyperparameter, the weights W^* that minimized the loss function from Equation 14 needs to be determined. In this work, the weights serve as the forcing-to-stiffness ratio elaborated in Section 3.2.

$$W^* = \min_W \sum_{i=1}^n L(f(x_i; W), y_i) \quad (14)$$

With $W = w_0, w_1, w_2, \dots, w_n$ being the collection of weights/hyperparameters to be solved from the system of equation, $f(x_i; W)$ is the predicted output of the model with respect to the initial weights, and y_i is the actual output desired in this case taken from a real measurement campaign.

In solving a system of equations in the form of $Ax=b$ overfitting is a highly desired characteristic in order to obtain the parameter that best describes the environmental factors, hence no training datasets used. The formula is shown in Equation 15 [19].

$$Ax = b + r = b_{true} \quad (15)$$

With $A = [a_{ij}] \in R^{m \times n}$ is the constant matrix model, in this work the matrix A defined in Equation 11. $b \in R^m$ is a vector containing model output or measurements, $b_{true} \in R^m$ is a vector

of true values, and $r \in R^m$ is vector of model error. An energy function that represents model error is defined in Equation 16 that serves as the objective equation that minimizes error with x :

$$E(x) = \sum_{i=1}^m \epsilon_i(r_i(x)) \quad (16)$$

To find x that minimizes the energy function, the gradient $\nabla E(x)$ must be calculated as defined in Equation 17. In this study, a modified version of gradient descent called Nesterov Accelerated Gradient Descent (NAG) is applied. NAG is known for accelerating the optimization process and reducing overshoot by incorporating a “lookahead” step in each iteration [20].

$$\nabla E(x) = \left[\frac{\delta E(x)}{\delta x_1}, \frac{\delta E(x)}{\delta x_2}, \dots, \frac{\delta E(x)}{\delta x_n} \right] = A^T (Ax - b) \quad (17)$$

3. Results and discussion

3.1 Case study

3.1.1 Wind turbine structure's specification overview

This work involves the modeling of a monopile structure with the main source of vibration is originated from gearbox on wind turbine *GE Wind Energy 1.5s Offshore* with its specification shown in Table 1 [21]. The monopile structure surface discretization sketch is shown in Figure 7.

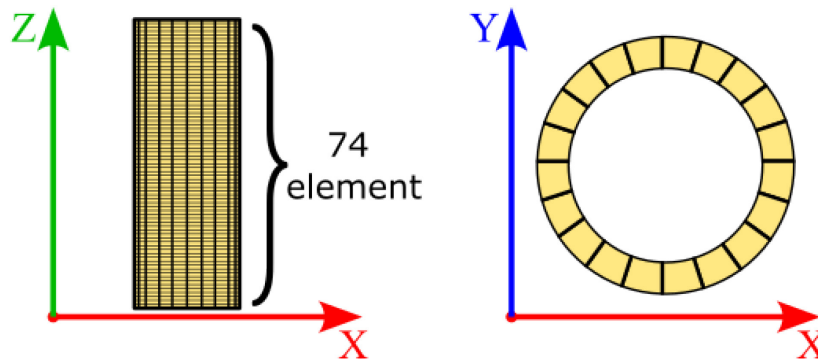


Figure 3. Monopile surface discretization: the structure is divided into 20 equal segments in the circumferential direction and 74 segments in the vertical direction.

3.1.2 Scope of the model

In modeling underwater acoustics using CHIEF, this study imposes several simplifying assumptions to address numerical limitations. The focus is on the structure's interaction with water, specifically the sound pressure transmitted directly to it, while other factors like compressional and shear waves in the sediment [22] are excluded. The model assumes a constant sound speed with depth and simplifies the seafloor profile to a flat 12.9 meters, matching the depth of Hydrophone 3 despite slight actual variation as summarized in Table 2. In this study, only the structure's surface boundary condition is considered, any other boundary conditions, such as bottom and surface reflection, and multiple turbine conditions are disregarded. Additionally, sea surface reverberation has been ignored, as sound waves interacting multiple times with the ocean surface and seabed is beyond the scope of this study.

Table 1. GE wind energy 1.5s offshore wind turbine and monopile structure specification.

Parameter	Value
Rated Power	1.425 MW
Number of blades	3
Rotor Diameter	70.5 m
Hub height	65 m
Cut in speed	3 m/sec
Cut out speed	25 m/sec
Rotor operation speed	11 – 20 rpm
Foundation type	Monopile
Nacelle weight	49,000 kg
Rotor weight	28,000 kg
Tower weight	76,000 kg
Transition piece weight	22,000 kg
Blade weight	5,216 kg
Gearbox ratio	90:1
Monopile dimension	3.65 m × 55 mm × 33.7 m
Monopile weight	165,000 kg

3.2 Mode contribution determination

Three hydrophones are used during the measurement campaign in Utgrunden wind farms [24], the location of each hydrophone relative to turbine 4, and its water depth are shown in Table 2. Hydrophone 3, the closest to the wind farm, was selected for analysis as it captured the highest signal resolution. The pressure level reading from turbine 4 while operating at wind speed 14 m/s is shown in Figure 4.

Table 2. Location of hydrophones relative to turbine 4 and their depth.

Hydrophone	Distance to turbine #4 (m)	Water depth (m)
Hydrophone 1	463	18.0
Hydrophone 2	160	15.2
Hydrophone 3	83	12.9

To calculate the excited vibration of the wind turbine, the dynamic contribution of the mode shape formula is utilized as shown in Equation 18. The term ξ_i/k_i is often named the forcing-to-stiffness ratio. No information regarding the forcing of the environment is available in this study; therefore ξ_i/k_i is assigned as R_i . Hence, the equation for the vibration velocity of the monopile surface can be expressed by Equation 19. The result of natural frequencies for the monopile structure are shown in Table 3.

The force-to-stiffness ratio ξ_i/k_i obtained from the gradient descent results are summarized in Table 4 and applied to Equation (19) to compare deviations from the reference sound levels shown in Figure 4, the comparison presented in Figure 5 shows a similar sound levels, with the largest differences at low frequencies due to environmental noise captured alongside structural vibrations. To simulate the primary noise contributor at 177 Hz, the results show a slight frequency shift, with 188.7 Hz being used to capture the dominant term instead of the original frequency.

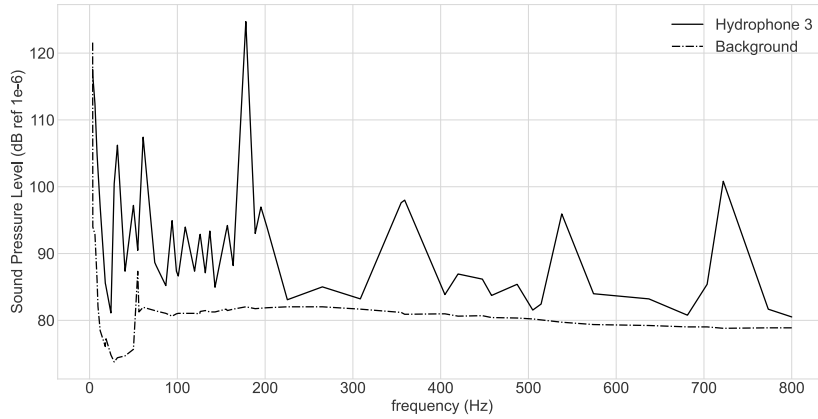


Figure 4. Hydrophone 3 recorded sound pressure levels from turbine 4 at 14 m/s wind speed, compared to background noise with no turbines operating.

$$\{x\} = \sum_{i=1}^{\infty} \left(\{\Phi\}_i \frac{\xi_i}{k_i} DAF_i \cos[\omega_i t] \right) \tag{18}$$

$$\{v\} = \sum_{i=1}^{\infty} (\omega_i \{\Phi\}_i R_i DAF_i \cos[\omega_i t]) \tag{19}$$

Table 3. Wind turbine mode frequencies using Euler-Bernoulli beam theory. Frequencies ranging from 1 up to 800 Hz following the basis of this study.

Mode Number	Frequency (Hz)	Mode Number	Frequency (Hz)
1	3.4806	12	225.31801
2	9.53077	13	265.23956
3	17.91222	14	308.47101
4	28.02358	15	355.00885
5	40.39122	16	404.85245
6	56.22984	17	457.99902
7	75.79421	18	514.45022
8	98.92243	19	574.20463
9	125.4884	20	637.26413
10	155.4292	21	703.62561
11	188.7112	22	773.29378

Table 4. The forcing-to-stiffness ratios acquired from the gradient descent algorithm described.

Mode Number	$\frac{\xi_i}{k_i}$	Mode Number	$\frac{\xi_i}{k_i}$
1	0.11350581	12	0.01095502
2	0.04186815	13	0.00213889
3	0.02525101	14	0.00183713
4	0.02715436	15	0.00548724
5	0.0020917	16	0.001278
6	0.00293712	17	0.00044378
7	0.00297696	18	-0.00118743
8	0.00380076	19	-0.00039723
9	0.00290444	20	-0.00031718
10	0.02623104	21	0.00210283
11	0.04467592	22	-0.00097174

3.3 Near-field pressure

3.3.1 Underwater acoustic attenuation per doubled distance comparison

Due to limitations previously described in Section 3.1.2, the outcomes of this study specifically concern to the depth wherein the effect of these two factors is least significant, which is in the mid-water depth. To approximate the attenuation rate in the same fashion as the actual measurement [24]. Figure 6 presents the distribution of modeled pressure level with distance. This spatial attenuation rate is applicable in all directions because of the symmetrical noise distribution. As shown in Table 5, the attenuation per doubled distance can be estimated to be around 3 dB to 6 dB which encompasses attenuation obtained from the actual measurement (4 dB) and attenuation in the cylindrical propagation model (3 dB) [23].

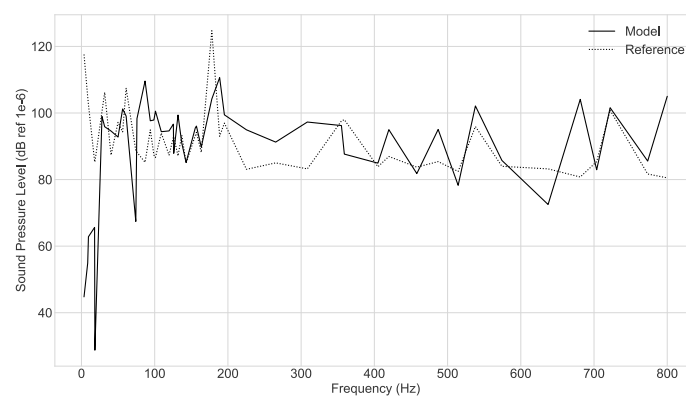


Figure 5. Pressure magnitude and sound pressure level comparison of natural and dominant frequencies compared to reference value from field measurement.

Table 5. Pressure level attenuation rate. Hyd3-Hyd2 denotes the attenuation that occurred between hydrophone 3 and hydrophone 2, and similarly for other pairs.

Frequency (Hz)	Attenuation per doubled distance (dB)		
	Hyd3-Hyd2	Hyd3-Hyd1	Hyd2-Hyd1
31.7	3.469	5.856	5.92
188.7	3.349	6.6	6.341
722.0	4.044	5.9	6
Average (dB)	3.621	6.11	6.087

4. Conclusions

The proposed method has shown a good approximation for the prediction of underwater noise using limited amount of data. Proven by its ability to predict acoustic noise attenuation. However, the achieved result is still far from perfect, and achieving a detailed noise 3D distribution can be challenging due to multiple factors such as sound speed profile, co-existing multiple frequency components, water surface and seabed reflection, and multiple turbine interaction. Therefore, a more complex boundary element model may be needed to be developed to tackle the problem statement. The proposed model improvement aims to account for sound wave interactions among multiple bodies within wind farm clusters and complex seafloor morphology, enhancing the understanding of wave patterns in the vicinity of wind farms.

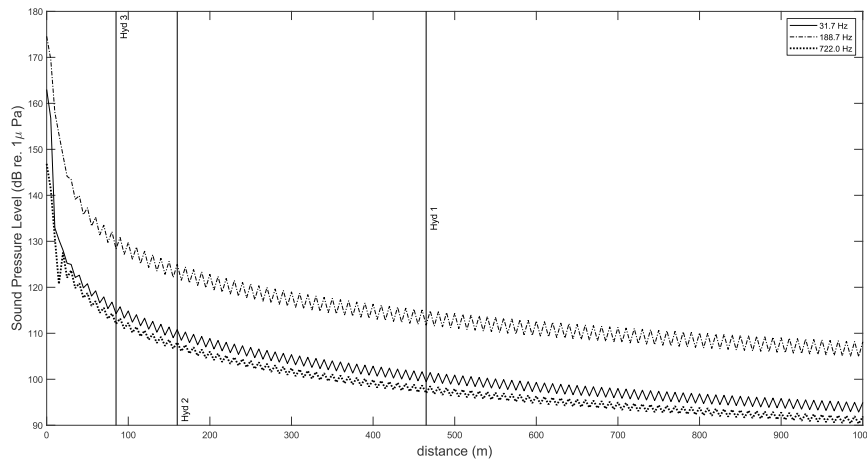


Figure 6. The sound pressure level distribution caused by one turbine in excitation frequency of 31.7, 188.7, and 722.0 Hz. The highlighted points correspond to the location of each hydrophone.

4.1 3D underwater acoustic distribution

The resulting offshore wind farms noise contour from the operation of the whole turbine is shown in Figure 7 [18] and its three dimensional plot is presented in Figure 8.

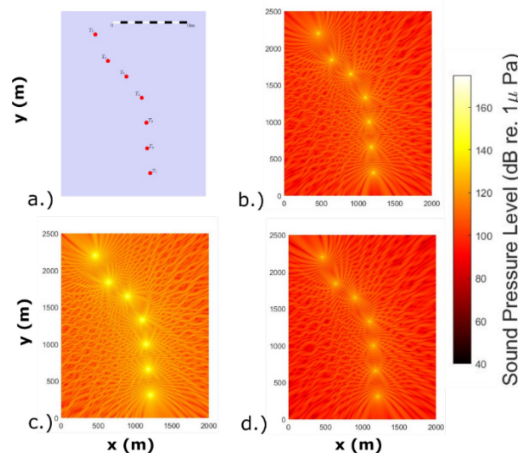


Figure 7. Mid-water depth sound pressure level distribution. (a) Actual wind farm layout, (b) Noise distribution at 31.7 Hz, (c) Noise distribution at 188.7 Hz, (d) Noise distribution at 722.0 Hz.

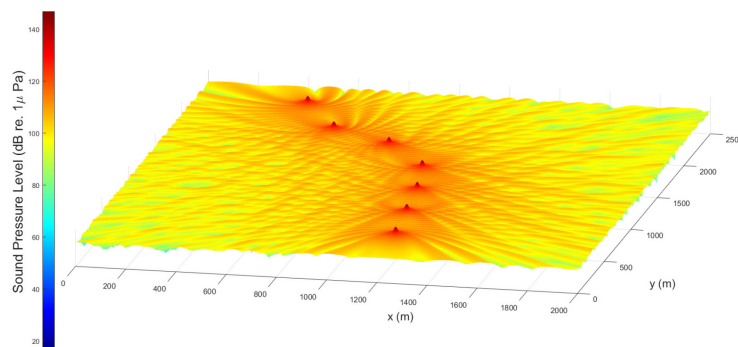


Figure 8. Mid-water depth sound pressure level distribution in isometric view. a) Sound pressure level distribution for dominant frequency 722.0 Hz.

Acknowledgements

Acknowledgement to Faculty of Civil and Environmental Engineering through P2MI (Research and Innovation Program), ITB Research Grant 2022.

References

- [1] J. Tougaard, O. D. Henriksen, and L. A. Miller, "Underwater noise from three types of offshore wind turbines: Estimation of impact zones for harbor porpoises and harbor seals," *J Acoust Soc Am*, vol. 125, no. 6, pp. 3766–3773, Jun. 2009, doi: 10.1121/1.3117444.
- [2] B. Marmo, I. Roberts, M. P. Buckingham, S. King, and C. Booth, "Modelling of Noise Effects of Operational Offshore Wind Turbines including noise transmission through various foundation types," 2013. Accessed: Mar. 16, 2023. [Online]. Available: https://tethys.pnnl.gov/sites/default/files/publications/Marmo_et_al_2013.pdf
- [3] J. Tougaard, L. Hermannsen, and P. T. Madsen, "How loud is the underwater noise from operating offshore wind turbines?," *J Acoust Soc Am*, vol. 148, no. 5, pp. 2885–2893, Nov. 2020, doi: 10.1121/10.0002453.
- [4] T. Pangerc, P. D. Theobald, L. S. Wang, S. P. Robinson, and P. A. Lepper, "Measurement and characterisation of radiated underwater sound from a 3.6 MW monopile wind turbine," *J Acoust Soc Am*, vol. 140, no. 4, pp. 2913–2922, Oct. 2016, doi: 10.1121/1.4964824.
- [5] K. Sathish, R. Anbazhagan, R. C. Venkata, F. Arena, and G. Pau, "Investigation and Numerical Simulation of the Acoustic Target Strength of the Underwater Submarine Vehicle," *Inventions*, vol. 7, no. 4, p. 111, Dec. 2022, doi: 10.3390/inventions7040111.
- [6] A. Purwana, I. M. Ariana, D. W. Handani, and W. Wardhana, "Performance and Noise Prediction of Marine Propeller Using Numerical Simulation," *IPTEK Journal of Proceedings Series*, vol. 4, no. 1, p. 20, Dec. 2018, doi: 10.12962/j23546026.y2018i1.3501.
- [7] A. Erturk and D. J. Inman, *Piezoelectric Energy Harvesting*. Wiley, 2011. doi: 10.1002/9781119991151.
- [8] B. Boukhezzer, L. Lupu, H. Siguerdidjane, and M. Hand, "Multivariable control strategy for variable speed, variable pitch wind turbines," *Renew Energy*, vol. 32, no. 8, pp. 1273–1287, Jul. 2007, doi: 10.1016/j.renene.2006.06.010.
- [9] C. Jauch, "A flywheel in a wind turbine rotor for inertia control," *Wind Energy*, vol. 18, no. 9, pp. 1645–1656, Sep. 2015, doi: 10.1002/we.1784.
- [10] D. T. Wilton, "Acoustic radiation and scattering from elastic structures," *Int J Numer Methods Eng*, vol. 13, no. 1, pp. 123–138, 1978, doi: 10.1002/nme.1620130109.
- [11] H. A. Schenck, "Improved Integral Formulation for Acoustic Radiation Problems," *J Acoust Soc Am*, vol. 44, no. 1, pp. 41–58, Jul. 1968, doi: 10.1121/1.1911085.
- [12] C. H. Wilcox, "A generalization of theorems of Rellich and Atkinson," *Proceedings of the American Mathematical Society*, vol. 7, no. 2, pp. 271–276, 1956, doi: 10.1090/S0002-9939-1956-0078912-4.
- [13] O. D. Kellogg, "The Potential," in *Foundations of Potential Theory*, Berlin, Heidelberg: Springer Berlin Heidelberg, 1967, pp. 160–164. doi: 10.1007/978-3-642-86748-4_3.
- [14] A. Lavie and A. Leblanc, "Integral equation methods with unique solution for all wavenumbers applied to acoustic radiation," *European Journal of Computational Mechanics*, pp. 619–636, Aug. 2010, doi: 10.13052/EJCM.19.619-636.
- [15] G. W. Benthien, D. Barach, and D. Gilette, "CHIEF User's Manual," Naval Ocean System Center, 1988.
- [16] P. Businger and G. H. Golub, "Linear least squares solutions by householder transformations," *Numer Math (Heidelb)*, vol. 7, no. 3, pp. 269–276, Jun. 1965, doi: 10.1007/BF01436084.
- [17] I. B. Crandall, "Theory of Vibrating Systems and Sound," 2015.
- [18] J. Nocedal and S. J. Wright, *Numerical Optimization*, vol. 2. Springer New York, 2006. doi: 10.1007/978-0-387-40065-5.
- [19] I. Kidil, "Neural Networks Solving Linear Systems - Chair of Scientific Computing," 2021. <https://www.cs.cit.tum.de/en/scs/news/scs-colloquium/article/iremnr-kidil-neural-networks-solving-linear-systems/> (accessed Mar. 16, 2023).
- [20] Y. Nesterov, *Introductory Lectures on Convex Optimization*, vol. 87. Boston, MA: Springer US, 2004. doi: 10.1007/978-1-4419-8853-9.
- [21] "Enron 1.5 s offshore - 1,50 MW - Wind turbine." <https://en.wind-turbine-models.com/turbines/91-enron-1.5-s-offshore> (accessed Mar. 16, 2023).
- [22] J. Amaral, K. Vigness-Raposa, J. H. Miller, G. R. Potty, A. Newhall, and Y.-T. Lin, "The Underwater Sound from Offshore Wind Farms", doi: 10.1121/AT.2020.16.2.13.
- [23] W. A. Kuperman and J. F. Lynch, "Shallow-Water Acoustics," *Phys Today*, vol. 57, no. 10, pp. 55–61, Oct. 2004, doi: 10.1063/1.1825269.
- [24] H. Lindell, "Utgrunden off-shore wind farm-Measurements of underwater noise," 2003. [Online]. Available: <https://www.researchgate.net/publication/275037654>